Decoupling of nanoindentation residual stress field in single-crystalline 4H-SiC via micro-Raman spectroscopy

Yang, Zhoudong; Tian, Jing; Wang, Xinyue; Chen, Junwei; Zuo, Yuanhui; Zhang, Rongjun; Tang, Hongyu; Fan, Xuejun; Zhang, Guoqi; Fan, Jiajie

DOI
10.1364/OL.563213

Publication date
2025

Document Version
Final published version

Published in
Optics Letters

Optics Letters

Decoupling of nanoindentation residual stress field in single-crystalline 4H-SiC via micro-Raman spectroscopy

Zhoudong Yang,[1] Jing Tian,[1] Xinyue Wang,[1] Junwei Chen,[1] Yuanhui Zuo,[2] Rongjun Zhang,[3] Hongyu Tang,[1] Xuejun Fan,[4] Guoqi Zhang,[5] and Jiajie Fan[1,2,5,*]

[1]Shanghai Engineering Technology Research Center for SiC Power Device, School of Intelligent Robotics and Advanced Manufacturing, Fudan University, Shanghai 200433, China
[2]Research Institute of Fudan University in Ningbo, Ningbo 315336, China
[3]School of Information Science and Technology, Fudan University, Shanghai 200433, China
[4]Department of Mechanical Engineering, Lamar University, PO Box 10028, Beaumont, Texas 77710, USA
[5]EEMCS Faculty, Delft University of Technology, Delft 2628, The Netherlands
*jiajie_fan@fudan.edu.cn

Received 24 March 2025; revised 25 April 2025; accepted 4 May 2025; posted 7 May 2025; published 19 May 2025

This Letter presents a combined analytical and experimental method to effectively decouple the radial and tangential residual stress fields induced by Berkovich nanoindentation in single-crystalline 4H-SiC using micro-Raman spectroscopy. By integrating the Raman stress characterization model with Yoffe's expanding cavity model, precise extraction of individual residual stress components around the indentation region is realized. Through the vertical backscattering micro-Raman mapping of the E_2 phonon mode, we systematically investigate the residual stress distribution near the indentation. The results highlight significant anisotropy in nanoindentation-induced stress fields, strongly dependent on the crystal orientation of 4H-SiC, predominantly featuring radial tensile stress gradients. This comprehensive theoretical–experimental approach offers a robust optical framework for residual stress characterization in 4H-SiC and provides foundational insights for extending Raman spectroscopy-based stress characterization to other crystalline materials and related device structures.

https://doi.org/10.1364/OL.563213

Silicon carbide (SiC) is a prominent third-generation semiconductor distinguished due to its wide bandgap, exceptional thermal conductivity, and remarkable chemical stability. It is vital for high-temperature electronics, high-power devices, and nuclear applications [1–4]. However, the inherent high hardness and elastic modulus of SiC often lead to substantial residual stresses during device fabrication processes. These stresses can degrade electrical performance and compromise long-term device reliability, especially under operational conditions involving combined thermal and electrical fields [5,6]. Therefore, accurately characterizing stress and strain distributions in single-crystalline 4H-SiC is critically important.

Nanoindentation is widely recognized as an effective technique for evaluating mechanical properties such as hardness and Young's modulus [7,8]. During nanoindentation, it induces plastic deformation, generating nonuniform residual stress fields around the indentation area. Detailed investigation and decoupling of these stress components provide critical insights into the fundamental mechanical responses of SiC. Nonetheless, comprehensive experimental studies addressing the anisotropic residual stress distribution in single-crystalline SiC remain scarce.

Micro-Raman spectroscopy probes lattice distortion and microscale stress via inelastic photon–phonon scattering, offering submicron spatial resolution, MPa-level sensitivity, and noncontact in situ measurement [9–11]. These capabilities give it advantages over XRD, ultrasonics, curvature, and birefringence methods for mapping residual stress in microregions, multilayer composites, and dynamic processes [12]. Previous work has employed Raman mapping to characterize residual stresses in 4H-SiC induced by ion implantation [13–15] and laser irradiation [16,17], but these studies generally adopt the in-plane equibiaxial stress model and thus overlook the potential inhomogeneity of the stress field. A few groups have combined finite-element simulations with Raman measurements to examine stress fields at SiC/Si and SiC/SiO_2 heterointerfaces [18,19], elucidating how lattice mismatch drives stress evolution. However, such approaches focus on interface-driven stress variations; the anisotropic stress components generated by local mechanical loading have not received sufficient attention. Decoupling these stress components under realistic machining conditions is critical for a deeper understanding of 4H-SiC's microscale mechanical behavior.

In this Letter, we introduce an integrated analytical and experimental approach that effectively decouples the radial and tangential residual stress fields resulting from Berkovich nanoindentation in single-crystalline 4H-SiC. By combining micro-Raman spectroscopy with Yoffe's expanding cavity model, we achieve precise identification and analysis of stress components

around the indentation site. Micro-Raman mapping of the E_2(TO) phonon mode demonstrates clear orientation-dependent anisotropy in the residual stress distributions, primarily manifesting as radial tensile gradients. This method advances the optical characterization framework for residual stress evaluation in 4H-SiC and provides a generalized analytical pathway for Raman-based stress assessments of other anisotropic crystalline materials.

The E_2(TO) phonon mode of 4H-SiC is highly sensitive to surface stress due to its vibration direction parallel to the (0001) plane; we selected this mode for analyzing and decoupling residual stress induced by nanoindentation. Firstly, we defined the crystal coordinate system with [1−100], [11−20], and [0001] orientations as the X, Y, and Z axes, respectively. Utilizing lattice dynamics and elastic theory, the specific equation between the 4H-SiC Raman phonon frequency shift and stress can be established [20]. Since the E_2(TO) mode of 4H-SiC is doubly degenerate, combined with the Raman selection law, the long-term equation of the lattice dynamics is simplified to [21]:

$$R^1_{E_2}=\begin{pmatrix}0&d&0\\d&0&0\\0&0&0\end{pmatrix}, R^2_{E_2}=\begin{pmatrix}d&0&0\\0&-d&0\\0&0&0\end{pmatrix},$$
$$\begin{vmatrix}\varepsilon_{uv}K_{uv11}-\lambda & \varepsilon_{uv}K_{uv12}\\ \varepsilon_{uv}K_{uv21} & \varepsilon_{uv}K_{uv22}-\lambda\end{vmatrix}=0. \quad (1)$$

Thus, the phonon frequency shift for E_2(TO) induced by the strain tensor components can be expressed as the following relationship:

$$\Delta\omega_{E_2}=a_{E_2}(\varepsilon_{xx}+\varepsilon_{yy})+b_{E_2}\varepsilon_{zz} \pm c_{E_2}\sqrt{(\varepsilon_{xx}-\varepsilon_{yy})^2+4\varepsilon_{xy}^2}, \quad (2)$$

where a_{E2}, b_{E2}, and c_{E2} are the phonon deformation potential (PDP) coefficients.

Under plane-stress conditions on the 4H-SiC wafer surface, generalized Hooke's law can be used to derive the deformation constitutive relationship. Incorporating this relationship into Eq. (2), the correlation between Raman frequency shift and stress components simplifies to [22]

$$\Delta\omega_{E_2}=a'_{E_2}(\Delta\sigma_{xx}+\Delta\sigma_{yy}) \pm c'_{E_2}\sqrt{(\Delta\sigma_{xx}-\Delta\sigma_{yy})^2+4\Delta\sigma_{xy}^2}, \quad (3)$$

where the specific equations of a_{E2}' and c_{E2}' in the formula are (s_{11}, s_{12}, and s_{13} are the components in the compliance coefficient matrix (S) of the sample):

$$a'_{E_2}=a_{E_2}(s_{11}+s_{12})+b_{E_2}s_{13}, \quad c'_{E_2}=c_{E_2}|s_{11}-s_{12}|. \quad (4)$$

Following Yoffe's expanding cavity theory, the residual stress fields induced by nanoindentation exhibit anisotropic distributions describable in a cylindrical coordinate framework. Figure 1(a) illustrates the orientation relationship between the Berkovich indenter and the (0001) plane of 4H-SiC, and Fig. 1(b) presents the defined crystal and cylindrical coordinate systems centered at the indentation site. In this cylindrical framework, the Z' axis aligns with the [0001] crystal direction of 4H-SiC, where r represents the radial direction and φ represents the angle measured counterclockwise from the [1−100] crystal direction.

Based on the Porporati and Pezzotti modified Yoffe's expanding cavity model, the individual stress components within the

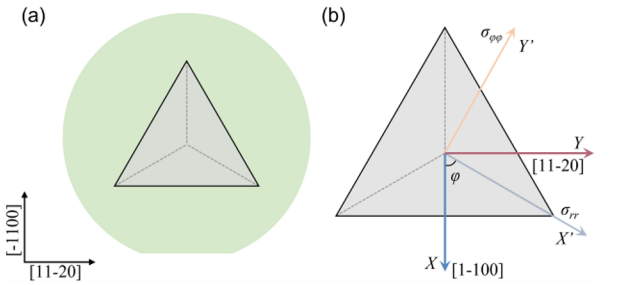

Fig. 1. (a) Schematic diagram of the Berkovich nanoindenter acting on the (0001) crystal plane of 4H-SiC. (b) Definition of the crystal and cylindrical coordinate systems based on the (0001) crystal plane.

indentation-induced residual stress field at any arbitrary point in the cylindrical coordinate system can be determined as follows [23] (for the full derivation, please refer to Eqs. (15)–(18) in Ref. [23]):

$$\Delta\sigma_{rr}=\frac{4B_{rr}}{r^3}(\nu_{r\varphi}-2),\ \Delta\sigma_{\varphi\varphi}=\frac{4B_{\varphi\varphi}}{r^3}(1-2\nu_{\varphi r}),$$
$$B_{rr}=0.102\frac{G_{rz}f_{\varphi\varphi}\sqrt[3]{\frac{P}{H}}}{\pi(1-2\nu_{\varphi r})},\quad B_{\varphi\varphi}=0.102\frac{G_{z\varphi}f_{\varphi\varphi}\sqrt[3]{\frac{P}{H}}}{\pi(1-2\nu_{\varphi r})}, \quad (5)$$

where r, φ, and z represent the radial, tangential, and axial (i.e., vertical plane) directions in this cylindrical coordinate system, respectively. Correspondingly, the radial stress component ($\Delta\sigma_{rr}$), tangential stress component ($\Delta\sigma_{\varphi\varphi}$), and shear stress component ($\Delta\sigma_{r\varphi}$) describe the local stress state, with $\Delta\sigma_{r\varphi}=0$ due to symmetry. Additionally, $\nu_{r\varphi}$ and $\nu_{\varphi r}$ represent Poisson's ratio; G_{rz} and $G_{z\varphi}$ denote shear modulus; B_{rr} and $B_{\varphi\varphi}$ characterize the extent of radial and tangential plastic deformation, and $f_{\varphi\varphi}$ denote the non-conservative plastic deformation factor near the indentation after plastic deformation. The peak load applied by the indenter is represented by P, and H indicates the Vickers hardness of the material.

If the radial-shear component is negligible ($\Delta\sigma_{r\varphi}=0$), the stress state around the indentation can be considered biaxial and anisotropic, with clearly defined principal stress directions. Therefore, the relationship between radial and tangential stress components can be directly expressed by their ratio:

$$\frac{\Delta\sigma_{rr}}{\Delta\sigma_{\varphi\varphi}}=\frac{G_{rz}(\nu_{r\varphi}-2)}{G_{z\varphi}(1-2\nu_{\varphi r})}=A. \quad (6)$$

Under vertical backscattering conditions and stress relationships defined in both the crystal and cylindrical coordinate systems with Eq. (3), the specific correlation between the $\Delta\sigma_{rr}$ and $\Delta\sigma_{\varphi\varphi}$ stress components and the Raman shift of the E_2(TO) phonon mode induced by nanoindentation on the (0001) crystal plane of 4H-SiC can be expressed as follows (the specific derivation of the correlation process is in Supplement 1):

$$\Delta\sigma_{\varphi\varphi}=\frac{\Delta\omega_{E_2}}{[a'_{E_2}(A+1)+c'_{E_2}|(A-1)(\cos^2\varphi-\sin^2\varphi)|]},$$
$$\Delta\sigma_{rr}=\frac{A\Delta\omega_{E_2}}{[a'_{E_2}(A+1)+c'_{E_2}|(A-1)(\cos^2\varphi-\sin^2\varphi)|]}. \quad (7)$$

To determine specific values of Poisson's ratio and shear modulus, we calculated the compliance coefficient matrix (S') of 4H-SiC in the cylindrical coordinate system through coordinate rotation. To simplify calculations, we set the basis vectors X_e, Y_e, and Z_e to align with the crystal coordinate system, respectively.

We then aligned the Z axis in the crystal coordinate system with the cylindrical coordinate system's Z' axis while rotating the X and Y axes accordingly to obtain the X' and Y' axes of the cylindrical coordinate system. The transformation matrix (T) from the crystal coordinate system to the cylindrical coordinate system is obtained as

$$\begin{pmatrix} X' \\ Y' \\ Z' \end{pmatrix} = T \begin{pmatrix} X_e \\ Y_e \\ Z_e \end{pmatrix} = \begin{pmatrix} \cos\varphi & \sin\varphi & 0 \\ -\sin\varphi & \cos\varphi & 0 \\ 0 & 0 & 1 \end{pmatrix} \begin{pmatrix} X_e \\ Y_e \\ Z_e \end{pmatrix}. \quad (8)$$

From this, we can obtain that S' in the cylindrical coordinate system is [24]

$$\begin{aligned} S' &= T_\varepsilon S T_\varepsilon^{\mathrm{T}}, \\ \varepsilon' &= T\varepsilon T^{\mathrm{T}} = T_\varepsilon \varepsilon, \end{aligned} \quad (9)$$

where ε' is the strain expression of the sample in the cylindrical coordinate system. T_ε represents the transformation matrix that converts strain components of the sample from the crystal coordinate system into the cylindrical coordinate system. The detailed expressions and solutions of the equations are provided in Supplement 1.

As shown in Fig. 1(b), the specific relationship between nanoindentation and crystal orientation is $\varphi = 60°$. Substituting into Eq. (9), S' is as follows (unit: $10^{-3}\,\mathrm{GPa}^{-1}$):

$$T_\varepsilon = \begin{pmatrix} \frac{1}{4} & \frac{3}{4} & 0 & 0 & 0 & \frac{\sqrt{3}}{4} \\ \frac{3}{4} & \frac{1}{4} & 0 & 0 & 0 & -\frac{\sqrt{3}}{4} \\ 0 & 0 & 1 & 0 & 0 & 0 \\ 0 & 0 & 0 & \frac{1}{2} & -\frac{\sqrt{3}}{2} & 0 \\ 0 & 0 & 0 & \frac{\sqrt{3}}{2} & \frac{1}{2} & 0 \\ -\frac{\sqrt{3}}{2} & \frac{\sqrt{3}}{2} & 0 & 0 & 0 & -\frac{1}{2} \end{pmatrix}, \quad (10)$$

$$S' = \begin{pmatrix} 2.08 & -0.43 & -0.16 & 0 & 0 & 0 \\ -0.43 & 2.08 & -0.16 & 0 & 0 & 0 \\ -0.16 & -0.16 & 1.858 & 0 & 0 & 0 \\ 0 & 0 & 0 & 6.30 & 0 & 0 \\ 0 & 0 & 0 & 0 & 6.30 & 0 \\ 0 & 0 & 0 & 0 & 0 & 5.02 \end{pmatrix}.$$

According to the definition of Poisson's ratio and shear modulus,

$$\begin{aligned} \nu_{r\varphi} &= -\frac{S'_{12}}{S'_{11}}, \ \nu_{\varphi r} = -\frac{S'_{21}}{S'_{22}} \\ G_{rz} &= \frac{1}{S'_{66}}, \ G_{z\varphi} = \frac{1}{S'_{55}}. \end{aligned} \quad (11)$$

This study investigates the relationship between crystal orientation and residual stress distribution induced by Berkovich nanoindentation on single-crystalline 4H-SiC. Nanoindentation tests were conducted on the (0001) crystal plane at room temperature, applying a maximum indentation depth of 600 nm at a constant loading rate of 10 nm s^{-1}. Indentations were performed at four randomly selected locations to ensure reliability, resulting in highly consistent overlapping loading–unloading curves, confirming uniformity in the measured elastic modulus and hardness across different test positions (Fig. 2).

Subsequently, micro-Raman mapping was employed to analyze the residual stress distribution surrounding the nanoindentation by evaluating shifts in the E_2(TO) phonon mode frequency (see Supplement 1, Fig. S2, for the peak position). As shown in Fig. 3, the mapping results indicate significant anisotropy in stress distribution near the indentation site. Specifically, the Raman frequency shift exhibited an initial increase followed by a gradual decrease when moving outward along the [1−100],

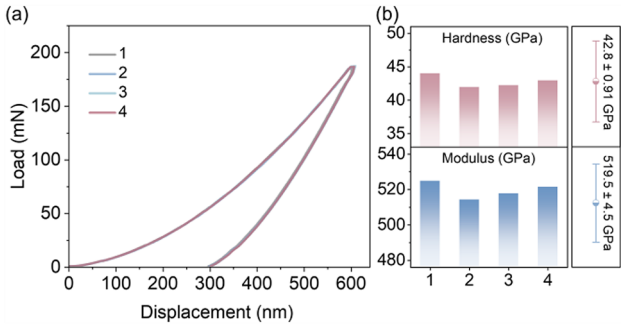

Fig. 2. (a) Force-displacement diagram of the (0001) crystal plane of 4H-SiC. (b) Hardness, elastic modulus, and error ranges (approximately 68.3% confidence level) from four parallel nanoindentation tests.

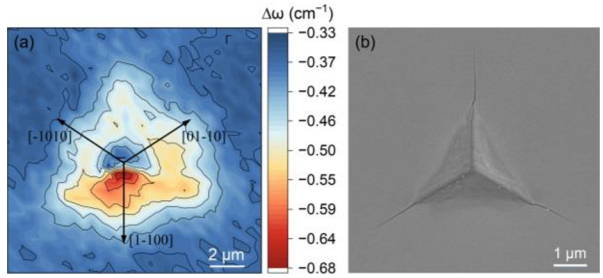

Fig. 3. (a) E_2(TO) phonon Raman frequency shift mapping distribution around the nanoindentation of the (0001) crystal plane of 4H-SiC. (b) Nanoindentation morphology of the (0001) crystal plane of 4H-SiC.

[−1010], and [01−10] crystal directions, with a maximum shift of approximately −0.68 cm^{-1} along the [1−100] orientation. Furthermore, distinct differences were observed in the frequency shift gradients among these orientations, displaying a notably slower decay along the [1−100] direction compared to the rapid decrease observed along the [−1010] and [01−10] directions.

Furthermore, the measured Raman shifts were converted into residual stress distributions using the established Raman–stress relationship (Eq. (7)). As shown in Fig. 4, the calculated residual stress fields reveal that stress distribution characteristics ($\Delta\sigma_{rr}$ and $\Delta\sigma_{\varphi\varphi}$) along different crystal orientations ([1−100], [−1010], [01−10]) align closely with Raman frequency shift trends, indicating that their distribution is affected by the nanoindenter geometry and the crystal orientation. Specifically, the stress gradient changes along the [1−100] direction are more obvious. The stress distribution shows that $\Delta\sigma_{rr}$ is predominantly tensile (positive value), reaching up to approximately 495 MPa, whereas the $\Delta\sigma_{\varphi\varphi}$ is mainly compressive (negative value), peaking at approximately −129 MPa. Notably, the radial stress magnitude is nearly four times greater than the tangential stress at identical locations, confirming the dominance of radial tensile stresses induced by nanoindentation on the surface of the 4H-SiC sample. This ratio is corroborated by the SEM image in Fig. 3(b), which shows cracks radiating from the indent along the radial direction. Mechanically, the Berkovich nanoindenter produces elastic–plastic deformation in 4H-SiC; during unloading, elastic recovery generates hoop tension that exceeds the lateral compression imposed by Poisson's effect [25]. Moreover, with one side of the indenter parallel to the [11–20] crystal direction

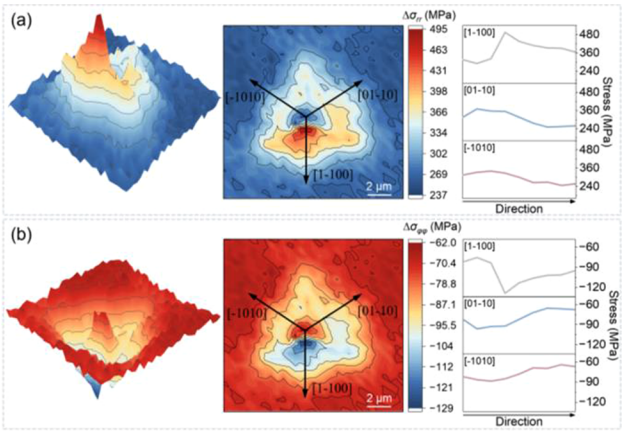

Fig. 4. (a) Mapping of the radial stress distribution around the indentation. (b) Mapping of the tangential stress distribution around the indentation. The line graphs show both radial and tangential stress magnitudes versus distance from the indentation center along the three marked crystal directions.

of the sample, the combination of indenter geometry and crystallographic elastic anisotropy concentrates the residual stress gradient along [1–100] [26]. Therefore, our Raman-derived residual stress distribution and crack morphology demonstrate the synergistic roles of indenter geometry and crystal orientation in governing local stress fields.

In summary, this study successfully decouples radial and tangential residual stress components at any positions near the nanoindentation on the (0001) crystal plane of 4H-SiC by integrating a Raman–stress characterization model with Yoffe's expanding cavity theory. Residual stress distributions obtained via vertical backscattering micro-Raman spectroscopy demonstrate anisotropic characteristics induced by nanoindentation, underscoring the critical importance of crystal orientation and nanoindenter geometry. This combined theoretical–experimental methodology not only advances optical residual stress analysis in 4H-SiC and offers guidance for optimizing device fabrication to minimize stress but also establishes a generalizable framework for detecting residual stresses in other anisotropic crystals (e.g., AlN, Ga_2O_3). Nonetheless, our conclusions are drawn under static loading and the assumption of negligible shear; extending this work to dynamic indentations and more complex stress states remains an important direction for future study.

Funding. National Natural Science Foundation of China (52275559, 62401157); Zhejiang Provincial Postdoctoral Science Foundation (ZJ2023118).

Disclosures. The authors declare no conflicts of interest.

Data availability. Data underlying the results presented in this Letter are not publicly available at this time but may be obtained from the authors upon reasonable request.

Supplemental document. See Supplement 1 for supporting content.

REFERENCES

1. X. Chen, X. Yang, X. Xie, *et al.*, Light: Sci. Appl. **12**, 28 (2023).
2. Z. Cheng, J. Liang, K. Kawamura, *et al.*, Nat. Commun. **13**, 7201 (2022).
3. C.-C. Tu, C.-L. Hung, K.-B. Hong, *et al.*, Nat. Rev. Electr. Eng. **1**, 435 (2024).
4. J. Chen, T. Tian, C. Gu, *et al.*, IEEE Trans. Power Electron. **99**, 1 (2025).
5. B. Hu, J. Ortiz Gonzalez, L. Ran, *et al.*, IEEE Trans. Device Mater. Reliab. **17**, 727 (2017).
6. H. Sakakima, A. Goryu, A. Kano, *et al.*, J. Appl. Phys. **128**, 025701 (2020).
7. L. Lyu, C. Song, Y. Wang, *et al.*, Adv. Mater. **37**, e2412635 (2025).
8. G. Man, Y. Jiang, and X. Wang, Adv. Funct. Mater. 0, 2425763 (2025).
9. L. Ma, X. Fan, and W. Qiu, Opt. Lett. **44**, 4682 (2019).
10. Z. Yang, X. Wang, W. Chen, *et al.*, Laser Photonics Rev. **18**, 2301300 (2024).
11. H. Yuan, P. Zhang, and F. Gao, Optica **8**, 1462 (2021).
12. J. Guo, H. Fu, B. Pan, *et al.*, Chin. J. Aeronaut. **34**, 54 (2021).
13. Q. Kang, X. Fang, C. Wu, *et al.*, Ceram. Int. **48**, 27076 (2022).
14. S. Yang, S. Tokunaga, M. Kondo, *et al.*, Appl. Surf. Sci. **500**, 144051 (2020).
15. K. Piskorski, M. Guziewicz, M. Wzorek, *et al.*, AIP Adv. **10**, 055315 (2020).
16. M. Rouhani, S. B. S. Metla, J. Hobley, *et al.*, J. Mater. Process. Technol. **338**, 118782 (2025).
17. H. Shi, Q. Song, Y. Hou, *et al.*, Ceram. Int. **48**, 24276 (2022).
18. N. Piluso, R. Anzalone, M. Camarda, *et al.*, J. Raman Spectrosc. **44**, 299 (2013).
19. M. Yoshikawa, M. Murakami, T. Ushida, *et al.*, J. Raman Spectrosc. **55**, 982 (2024).
20. L. Ma, W. Qiu, and X. Fan, Microelectron. Reliab. **118**, 114045 (2021).
21. X. Qin, X. Li, X. Chen, *et al.*, J. Alloys Compd. **776**, 1048 (2019).
22. Z. Yang, X. Wang, Y. Zuo, *et al.*, Laser Photonics Rev. **19**, 2401033 (2025).
23. A. A. Porporati and G. Pezzotti, Phys. Status Solidi A **208**, 1093 (2011).
24. I. De Wolf, J. Appl. Phys. **118**, 053101 (2015).
25. B. Zhu, D. Zhao, H. Zhao, *et al.*, Ceram. Int. **45**, 5150 (2019).
26. Z. Ni, Z. Chen, G. Chen, *et al.*, Appl. Phys. A **131**, 206 (2025).